Distribution Agreement

In presenting this thesis as a partial fulfillment of the requirements for a degree from Emory University, I hereby grant to Emory University and its agents the non-exclusive license to archive, make accessible, and display my thesis in whole or in part in all forms of media, now or hereafter now, including display on the World Wide Web. I understand that I may select some access restrictions as part of the online submission of this thesis. I retain all ownership rights to the copyright of the thesis. I also retain the right to use in future works (such as articles or books) all or part of this thesis.

Jipeng Yue April 13, 2020

Redox cycling and electrochemical features of copper-amyloid conjugates

by

Jipeng Yue

David G. Lynn, Ph.D.
Adviser

Department of Chemistry

David G. Lynn, Ph.D.

Adviser

Jen Heemstra, Ph.D.

Committee Member

Eri Saikawa, Ph.D.

Committee Member

2020

Redox cycling and electrochemical features of copper-amyloid conjugates

By

Jipeng Yue

David G. Lynn, Ph.D.

Adviser

An abstract of
a thesis submitted to the Faculty of Emory College of Arts and Sciences
of Emory University in partial fulfillment
of the requirements of the degree of
Bachelor of Arts with Honors

Department of Chemistry

2020

Abstract

Redox cycling and electrochemical features of copper-amyloid conjugates

By Jipeng Yue

Metalloproteins demonstrate the ability to perform novel reactions in biology, with even more potential functions stemming from protein engineering. Common laccases serve as examples of metalloproteins capable of performing redox catalysis on a variety of substrates. However, the lack of optimization, scalability and structural fidelity for common laccases limit their application within industrial settings. As a result, we looked towards an amyloid model in providing a scalable, green electrocatalyst. The resulting assembly, H-HHAQLVFFA-NH_2, can be co-assembled with Cu(II) ions to generate a ribbon assembly at different timescales than unmetallized K16A. The resulting assembly exhibits a highly elevated reduction potential and can perform hydrogen peroxide evolution.

Redox cycling and electrochemical features of copper-amyloid conjugates

By

Jipeng Yue

David G. Lynn, Ph.D.

Adviser

A thesis submitted to the Faculty of Emory College of Arts and Sciences
of Emory University in partial fulfillment
of the requirements of the degree of
Bachelor of Arts with Honors

Department of Chemistry

2020

Acknowledgements

I would like to thank all the members of the Lynn lab for their contributions and help towards the completion of this manuscript. Special thanks to Dr. David Lynn, Anthony Sementilli, and Youngsun Kim for their guidance. Additionally, we are grateful to NSF CHE-1507932 for supplying personnel, supplies, equipment, and additional resources for this research to be possible.

I offer my unconditional gratitude towards my parents, Dr. Cuiyong Yue and the late Dr. Han Bo, to whom I dedicate this thesis to *in memoriam*.

Table of Contents

Introduction……..1

Materials and Methods……4

Results……7

Discussions……15

References Cited……18

INTRODUCTION

Since the 1950s, when the X-ray characterization of sperm whale myoglobin revealed the presence of an iron atom within the protein, metalloproteins have garnered significant amounts of research interest.[1] In biology, metalloproteins account for about half of all proteins, with further estimates indicating that one quarter to one third of all proteins necessitate metal ions to carry out their functions.[2] Due to the complex metal-ligand interactions within their active sites, metalloproteins are capable of catalyzing difficult, multi-step reactions, such as respiration, photosynthesis, and biosynthesis of complex biochemical products, such as lipotic acid and biotin.[3-5]

Protein engineering has allowed for the expansion of metalloprotein functionalities, along with optimizations of existing catalytic functions.[6-7] One instance of metalloprotein function expansion comes from recent research, which indicate the potential of metalloproteins to act as a hydrogel that allow for heavy metal sequestration of specific metals from seawater, thus acting as an effective environmental hazard remover.[8] Recent scientific developments using metal substitution and directed evolution allowed for the development of metalloprotein catalysts capable of enantioselective C-H functionalization.[9]

Laccase, a cupredoxin superfamily member within numerous plants, fungi, and bacteria serves as one biological example of a metalloprotein catalyst.[10] The presence of a tricopper active site within laccase, comprised of type II and III copper complexes, allow it to perform one-electron oxidations for various polymers, such as phenols, polycyclic aromatic hydrocarbons, and plastics.[11-14] One substrate that laccase readily degrades is lignin - a large biopolymer that serve as building blocks in cell walls, wood,

and bark.[15] As a result, the ability of laccase to degrade lignin has been researched for industrial viability in paper processing and biofuel remediation.[16-17]

Beyond its application in lignin bioremediation, the tricopper active site of common laccases allow for the oxidation of a variety of substrates.[18] More importantly, laccase can be dubbed a green catalyst, due to the enzyme only requiring oxygen molecules as reactants, while only producing water molecules as byproducts.[19] Furthermore, with selective active sites and reduction potential range of ~400 mV – 800 mV, common laccases have the potential to act as green catalysts for selective oxidation of various substrates with high industrial relevance.[20]

Despite the numerous potential benefits of laccase catalysis, there are numerous weaknesses in the application of laccase to beneficial uses. Currently, optimization for robust laccase activity has not been elucidated.[21] Furthermore, the instability of fungal laccase due to minor temperature and pH changes, which are the strongest oxidizers, limit their practicality within industrial settings.[22] Lastly, current isolation of laccase stems primarily from production within bacteria, which involves inserting a desired vector for laccase expression.[23] As a result, there existed a knowledge gap in an easily scalable, green biocatalyst that is similarly oxidizing to common laccases.

To address this gap, we looked towards utilizing an amyloid model for a solution. Amyloids are aggregates of proteins with fibrillar structure, capable of self-assembling from monomeric peptides to larger order structures.[24] Amyloid fibrils traditionally adopt a cross-beta diffraction pattern, in which an extended beta-sheet with individual beta-strands being arranged perpendicular to the long axis of the fiber.[24] Notably, x-ray crystallography of cross-beta amyloid structures produce characteristic diffraction

signals at 4.7 and 9.8 Å, which corresponds to the inter-strand hydrogen bonding and lamination distances, respectively.[25] In addition, amyloids are infamous in the pathogenesis of numerous diseases, such as Alzheimer's Disease, Parkinson's Disease, Type I and II Diabetes, and fatal familial insomnia.[26] More recent developments have expanded the functionality of amyloids beyond pathogenic peptides. For instance, amyloid engineering allowed for the development of amyloid catalysts for stereoselective retro-aldol cleavage, self-assembling scaffolds for light harvesting and energy storage, and MOF-like nanomaterial analogues.[27-29]

One feature of amyloids is their disruption of metal ion homeostasis by internal metal sequestration.[30] As a result, amyloids can produce pseudo-metalloproteins capable of performing redox chemistry. For instance, Aβ(1-42) – the primary sequence for Alzheimer's Disease amyloid plaques – sequesters copper with high affinity and reduces free oxygen to produce H_2O_2.[31] As a result, Cu-Aβ(1-42) is considerably more cytotoxic than unmetallized Aβ(1-42).[31]

Our lab has engineered and synthesized a modified amyloid sequence capable of metal sequestration with great yield. The sequence, H-HHQALVFFA-NH_2 (K16A), assembles into fibers upon maturation within a week.

Due to its sequential brevity, K16A can be synthesized on a conventional microwave peptide synthesizer with high yield. Furthermore, K16A demonstrates strong solubility in various buffer environments. With respect to its metal chelation, historically similar sequences have suggested that K16A potentiates the chelation of metal with a 1:2 metal to peptide ratio. This suggests the potential Cu-K16A to have several Cu ions within its peptide array. Factoring in its molar mass of roughly 1 kDa, it has a higher

ratio of active site to molar mass ratio than compared to common laccases, which contains one active site in their 50-70 kDa total mass. In addition, K16A demonstrates reduced cytotoxicity than compared to Aβ(1-42), allowing for potential viability within biological, *in vivo* applications.[32] Coupled with previous knowledge on elevated reduction potentials of metals within amyloid systems, along with Cu-amyloid system redox activity, we hypothesized an elevated reduction potential and oxygen reductivity by Cu arrays, upon the maturation of Cu-K16A. In the following manuscript, we explored the structure, maturation conditions, and redox chemistry features of K16A and other amyloid analogues to address our hypothesis.

MATERIALS AND METHODS

Peptide Synthesis and Purification

Peptide synthesis was performed by standard FMOC solid-phase chemistry on the CEM Liberty Microwave Automated Peptide Synthesizer with FMOC Rink-amide polystyrene resin (AnaSpec. Inc). Crude peptides were isolated from their solid support through a cleavage cocktail composed of 95% trifluoroacetic acid (TFA) and various scavenger components (5% thioanisole, 2% anisole, 3% ethanedithiol) and isolated by ether extraction, repeated 3 times. The crude peptide pellet was dried overnight in a vacuum desiccator.

Crude peptide was purified through a Jasco Analytical Instrument High Performance Liquid Chromatography (HPLC, Easton, MD, USA) with an Atlantis dC18 column from Waters (Milford, MA, USA), using a 15%-85% H_2O/MeCN elution gradient

at 20 mL/min. Purity of the peptide was confirmed by MALDI-TOF analysis with a α-cyano-4-hydroxycinnamic acid (CHCA) matrix.

Transmission Electron Microscopy

10 µL of 2 mM peptide assemblies were added onto holey carbon grids (200 mesh. After peptides were absorbed and dried onto their respective grids for 1 minute, the excess peptide solution was removed using filter paper. A solution of 10% w/v uranyl acetate was added to the grids to stain the TEM grids for 1 minute before removal of excess stain with filter paper. The grids were placed back into their respective plastic containers and left to dry overnight at room temperature. The staining solutions were prepared fresh prior to staining to reduce staining artefacts. TEM micrographs were taken with a Hitachi HT-7700 TEM with magnifications between 10,000x-25,000x with a Tungsten filament at an accelerating voltage of 80 kV.

Amplex Red Assay

H_2O_2 generation from $CuCl_2$ was measured using the Amplex Red-horseradish peroxidase (HRP) method (Thermo Fischer Scientific, Waltham, VA). In the presence of H_2O_2, HRP catalyzes Amplex Red into fluorescent resorufin. Resorufin fluorescence was excited at 545 nm and detected at an emission wavelength of 590 nm using a SpectraMax iD3 Multi-Well Plate Reader with SoftMax Pro 7.0.3 software. Samples were subjected to shaking for 5 seconds before the first reads. No software-recommended optimizations were applied to sample collections. Assays were performed at room temperature with 96-well plate from Corning Costar. All collected data was fitted and plotted on OriginPro 8.0.

Peptide Assembly

2 mM K16A peptides were dissolved in a 25 mM MES buffer. The 25 mM MES buffer was constructed from a 1:1 ratio of metal-free water to 50 mM MES buffer. The peptide was first exposed to a half-volume of water, and then the remainder volume of 50 mM MES was subsequently added and diluted down to the final 25 mM concentration. For Cu(II)-K16A systems, equimolar $CuCl_2$ salt to peptide was titrated into the 50 mM MES buffer. Peptides were gently vortexed and rested until assembly maturation, monitored by circular dichroism minima transitions.

Circular Dichroism

Circular dichroism spectra were obtained on a Jasco J-1500 CD spectropolarimeter at room temperature. Spectra were collected between 260 nm to 190 nm at a scan rate of 50 nm/s. A quartz cuvette with a path length of 0.1 mm was used across all samples for spectra measurement with a step size of 0.2 mm. Three cycles were accumulated and averaged automatically for each individual spectrum. Data was fitted using a Boltzmann distribution on OriginPro 8.0.

Cyclic Voltammetry

Cyclic voltammetry experiments was performed on a WaveDriver Potentiostat with a standard three-electrode setup, which comprised of an Ag/AgCl reference electrode, a Pt counter electrode, and a glassy carbon working electrode. The glassy carbon working electrode was polished before and after voltammogram collection. A buffer of 25 mM MES, pH 5.6 with 200 mM KCl of supporting electrolyte was used for K16A models and $CuCl_2$, while a 25 mM HEPES and 10 mM NaCl buffer at pH 7.4 with

200 mM KCl was used for H14A. Cyclic voltammograms were collected at speeds of 25, 50, 100, 250, 500 mV/s for eight segments at each scan rate, with a potential range of -0.500 V to 0.600 V. Background scans of the various buffers were performed prior to experimental sample scans to ensure background minimization of buffer contribution. Data was collected on AfterMath 1.5.98 and plotted on OriginPro 8.0.

RESULTS

Generation of amyloid and copper-amyloid nanostructures can be achieved by FMOC chemistry solid-phase peptide synthesis.

The generation of our model sequence, K16A, required the use of solid-phase FMOC chemistry peptide synthesis, in which amino acids polymers are created sequentially on a solid support and removed after further purification. K16A was observed to form homogeneous fibrillar structures by TEM (Figure 1A).

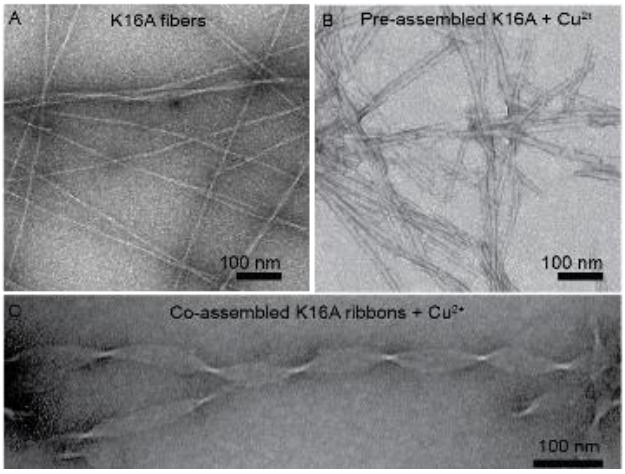

Figure 1. TEM images of K16A and Cu(II)-K16A assemblies. (A) Matured 1 mM K16A fibers. **(B)** Thickened fibers of matured pre-assembled 1 mM K16A with equimolar $CuCl_2$. **(C)** and matured ribbons of co-assembled 1 mM K16A with equimolar CuC_{l2}. All samples were assembled in pH 5.6, 25 mM MES at room temperature.

Further observations indicated the formation of thicker fibrils upon the addition of equimolar $CuCl_2$ salt to pre-assembled K16A (Figure 1B). However, upon incorporation of $CuCl_2$ during K16A assembly maturation, the resulting structures appear to be ribbons (Figure 1C). Characteristic amyloid cross-beta diffraction patterns of 4.9 and 9.8 Å, corresponding to the hydrogen bonding axis and lamination distance was observed in Cu(II)-K16A by pXRD (Figure 2A-B).

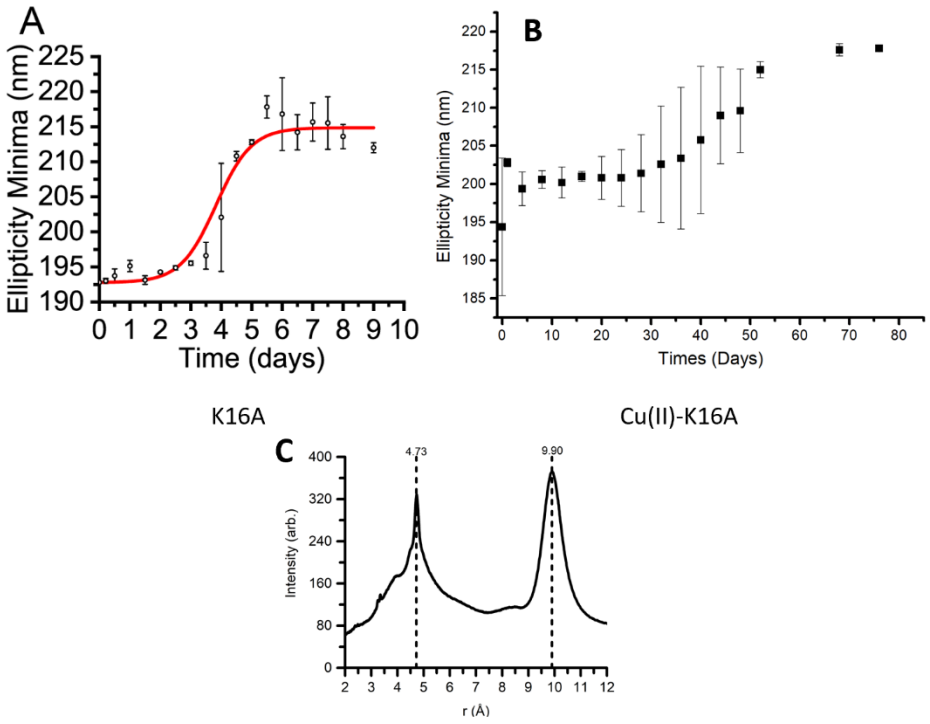

Figure 2. Co-assembled Cu(II)-K16A forms mature assemblies slower than K16A. (A-B) Cyclic dichroism scans of K16A and co-assembled Cu(II)-K16A assemblies during maturation. **(C)** pXRD diffraction patterns of co-assembled Cu(II)-K16A with distinct cross-beta features.

The timescale of K16A assembly rate also changed dramatically upon K16A co-assembly, as indicated by the change in circular dichroism ellipticity minima of K16A of 3.8 + 0.17 days to that of Cu(II)-K16A of 45 days (Figure 2C). However, peptide

assemblies with defined order and structure can be observable for both K16A and Cu(II)-K16A by 1 week and at 1 month timepoints by TEM (Figure 3a-d). Heterogeneous structures are observed upon assembly maturation in K16A, as demonstrated by the appearance of both fibers and helical ribbons at the 1-month time point (Figure 3A-B). Cu(II)-K16A demonstrates consistent homogeneity in peptide assemblies, as only ribbons are observable at the 1 month time point (Figure 3c-d).

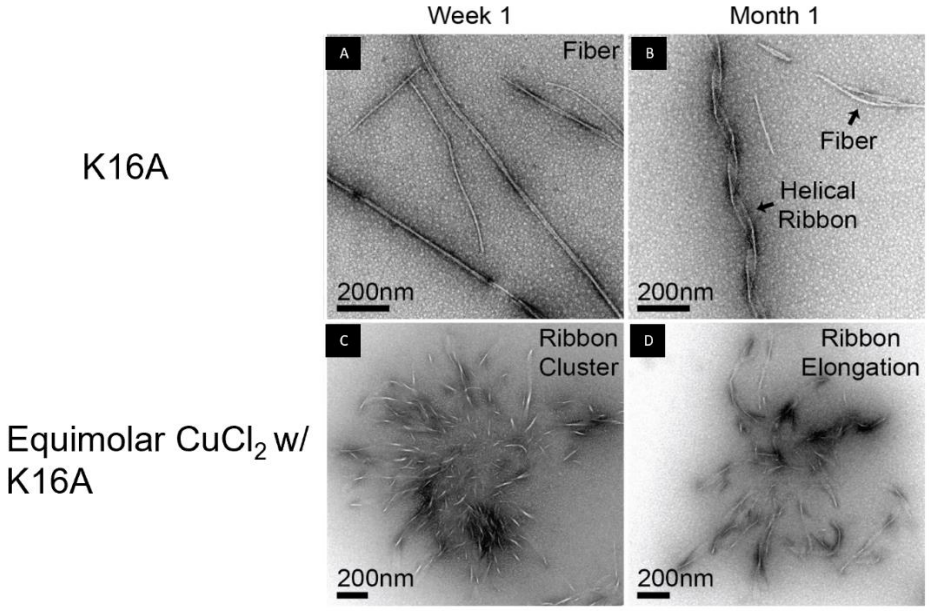

Figure 3. TEM images of K16A and co-assembled Cu(II)-K16A during maturation. (A-B) Images of 1-week and 1-month time point of K16A maturation. **(C-D)** Images of 1-week and 1-month time point of co-assembled Cu(II)-K16A maturation. All samples were assembled in pH 5.6, 25 mM MES at room temperature.

Co-assembled Cu(II)-K16A and preassembled Cu(II)-K16A both demonstrate slow electron transfer kinetics but demonstrate differing electrochemical reversibility.

Cyclic voltammetry (CV) was performed on K16A, co-assembled and pre-assembled K16A to probe the electrochemical capabilities of the peptide assemblies, along with their fidelity to undergo multiple redox cycles (Fig). Both co-assembled and pre-assembled Cu(II)-K16A present with broad waveshapes during Cu(II) reduction and Cu(I) reduction, indicating slow electron transfer kinetics. Furthermore, both co-assembled and pre-assembled Cu(II)-K16A demonstrate consistent waveshapes across all scan rates. However, the voltammogram of pre-assembled Cu(II)-K16A lacks a reverse wave with an anodic peak located near a potential of 400 mV, which indicates the chemical irreversibility. Meanwhile, Cu(II)-K16A contains a symmetric voltammogram with visible anodic and cathodic peaks, which suggest chemical reversibility and redox stability.

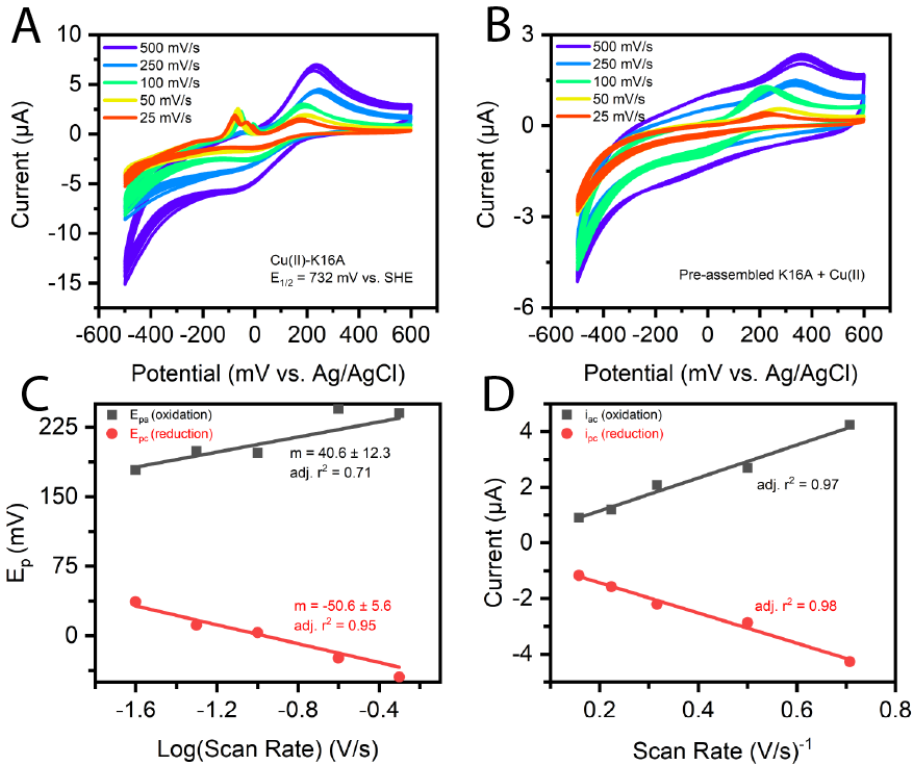

Figure 4. Co-assembled Cu(II)-K16A demonstrates electrochemical reversibility with slow electron transfer kinetics. (A-B) Cyclic voltammograms of co-assembled

and preassembled Cu(II)-K16A. **(C)** Co-assembled Cu(II)-K16A's peak potential vs. log(v) relationship **(D)** Cottrell relationship for co-assembled Cu(II)-K16A. All graphing and fits were performed on OriginPro 8.0.

When the peak potential of co-assembled Cu(II)-K16A plotted against the log of the scan rate, a linear relationship between the two measurements is observed, thus supporting the slow electron transfer kinetics of pre-assembled Cu(II)-K16A. In addition, chemically irreversible oxidation waves present themselves in the voltammogram of co-assembled Cu(II)-K16A at -0.033 V and -0.078 V with increasing broadness and decreased peak magnitude by scan speed, which we suggest to be the reduction of O_2 to H_2O_2 as suggested by contemporary literature. The Cottrell relationship of co-assembled Cu (II)-K16A appears strongly linear, which suggests electrochemical reversibility (Figure D).

Co-assembled Cu(II)-K16A demonstrates elevated electrochemical activity and reduction potential compared to CuCl2 in buffer and co-assembled Cu(II)-K16A particles.

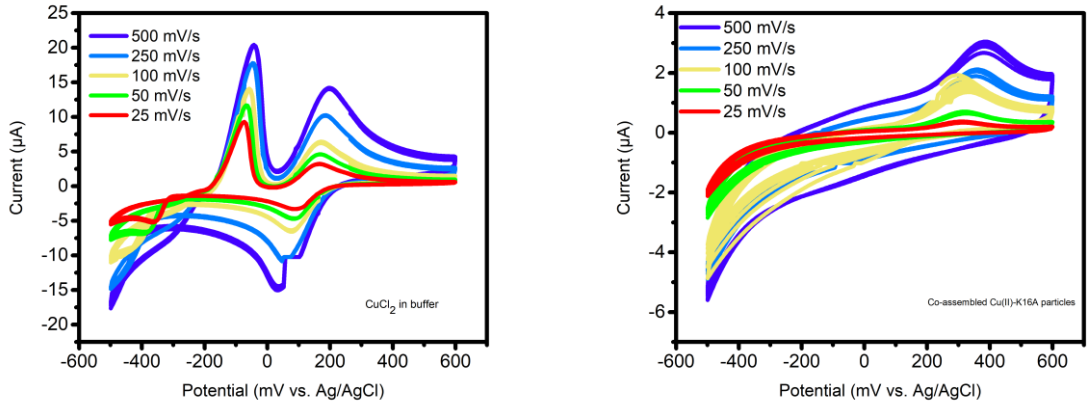

Figure 5. Electrochemical activity for Cu(II/I) within buffer and Cu(II)-K16A in buffer. (A) Cyclic voltammogram of $CuCl_2$ in buffer. **(B)** Cyclic voltammogram of co-assembled Cu(II)-K16A particles.

In order to determine the role of assembled K16A on the electrochemical activity of copper, we used $CuCl_2$ and co-assembled Cu(II)-K16A particles as negative controls for peptide-metal interactions and degree of assembly maturation, respectively. CV was performed on $CuCl_2$ and co-assembled Cu(II)-K16A particles (Figure 5A-B). From the voltammograms, both $CuCl_2$ and co-assembled Cu(II)-K16A particles displayed stable redox cycling with consistent waveshapes across all cycles. A reduction potential of 115 mV against an Ag/AgCl electrode, or 403 mV when compared against a standard hydrogen electrode (SHE) for $CuCl_2$ in buffer was ascertained for Cu(II) in solution. Co-assembled Cu(II)-K16A particles displayed slow electron transfer kinetics due to the broadness of the waveshape, along with a corresponding high reduction potential necessary for peaks to occur, suggests a chemically irreversibility within the particles. Like the voltammogram of co-assembled K16A, a broad peak between -0.230 mV to -0.108 mV is visible for $CuCl_2$'s voltammogram, with increasing current magnitude proportional to scan speed.

Within K16A, a bilayer system, Cu(II) presents differing electrochemical capabilities than within the monolayer system, H14A.

Since K16A is a bilayered peptide, we hypothesized that Cu ions could imbed within the inner leaflet of the bilayer, thus affecting its electrochemical potential from potential diffusion limitations. To test our hypothesis, we constructed a previously defined monolayer model peptide, H-HAQKLVFFA-NH_2 (H14A).

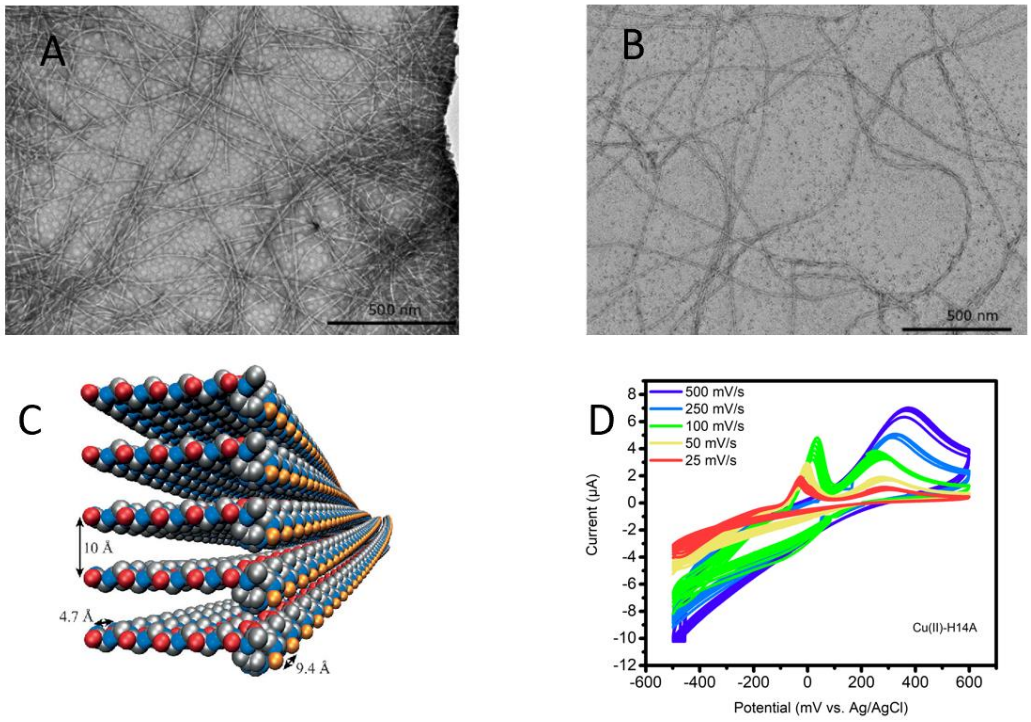

Figure 6. Assembly and electrochemical features of H14A. (A) TEM image of H14A particles and fibers after assembly and maturation. **(B)** TEM image of Cu(II)-H14A particles and fibers after assembly and maturation. **(C)** Cartoon structural render of H14A with amyloid lamination and hydrogen bonding axis distances. **(D)** Cyclic voltammogram of Cu(II)-H14A. All peptide assemblies above were performed in 25 mM HEPES + 10 mM NaCl at pH 7.4.

H14A assembles into a parallel, in-register monolayer (Figure 6A). In addition, TEM observes the formation of fibers in both H14A and Cu(II)-H14A upon maturation (Figure 6B-C). Cyclic voltammetry was performed on Cu(II)-H14A assembly to determine the electrochemical activity of the system. The resulting waveshape was broad, which suggests slow electron transfer kinetics. Furthermore, the voltammogram presented with an anodic peak located at a high potential and no visible cathodic peak, thus indicating chemical irreversibility within the system (Figure 6D). Like the voltammograms of $CuCl_2$ and co-assembled Cu(II)-K16A, a broad peak at -0.150 V is

present with increasing magnitude in relation to scan speed. The peak disappears at scan rates of 250 mV/s and 500 mV/s, most likely due to the scan rate outspeeding the electron transfer of the system at the corresponding peak potential.

Cu(I)-K16A can produce H_2O_2 at a faster rate than aquo-copper.

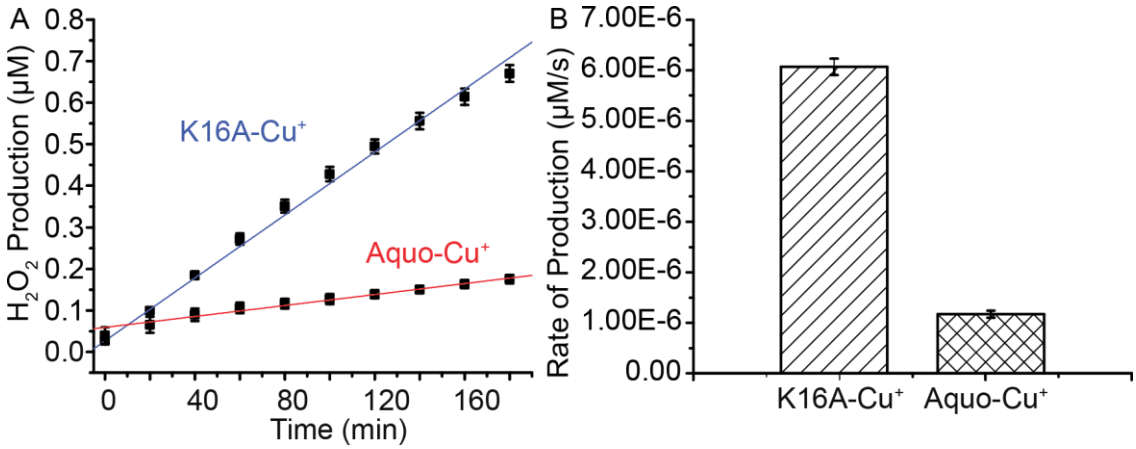

Figure 7. Cu(I)-K16A produces H_2O_2 at a faster rate than aquo-Cu(I) by Amplex Red assay. (A) Concentration of H_2O_2 produced by Cu(I)-K16A and aquo-Cu(I) over time. **(B)** Rate of H_2O_2 production by Cu(I)-K16A and aquo-Cu(I). Figure adapted from the thesis of Tolulope O. Omsun.

To compare and determine the rate of Cu(I)-K16A H_2O_2 production against aquo-Cu(I), an Amplex Red assay was performed for the detection of H_2O_2. The assay relies on the reduction of Amplex Red to resorufin by horseradish peroxidase in the presence of H_2O_2, which produces a fluorometric response. From the assay, it was determined that Cu(I)-K16A demonstrates significantly elevated rate of H_2O_2 production from aquo-Cu(I), thus implying the increased reduction potential of Cu(I)-K16A from aquo-Cu(I).

DISCUSSION

The study aimed to uncover the electrochemical potential of Cu(II)-K16A as a green, scalable, highly-oxidizing electrocatalyst, with inspiration to mimic the oxidation performed by common laccases. We hypothesized that if K16A forms amyloid fibrils with several Cu binding sites, then the resulting Cu array should have an elevated reduction potential and oxygen reductivity. However, due to the COVID-19 pandemic, numerous scheduled and progressing experiments were interrupted.

Previous amyloid sequences that our lab examined, such as H14A, demonstrates that short sequence peptides can incorporate copper with high density; For H14A, the peptide was able to sequester copper at 2:1 ratio of peptide to copper, thus incorporating copper with significantly higher density than common laccases.[31,33-34] Since the sequence of H14A only contains a one-amino acid difference from that of K16A, we assume that K16A contains the same capability of high-density copper sequestration. From the TEM images of co-assembled and preassembled Cu(II)-K16A, we saw a change in morphology in K16A from fibers to ribbons and wider fibers, respectively, upon introduction of metals. As a result, we can assume that high density, copper-amyloid interactions are occurring, which causes global morphological changes in the copper-amyloid system.

Further evidence of copper-amyloid interactions can be drawn from the dramatic difference in assembly maturation of K16A upon co-assembly with Cu(II), as demonstrated by CD plots of K16A and co-assembled Cu(II)-K16A maturation. Prior papers suggested that copper acts as a structural disruptor to bundle amyloid monomers, thus preventing assembly.[31] However, the previous studied examined

copper-amyloid assemblies within classic amyloid timescales of 24-168 hr. The highly elevated, 2-month maturation time of Cu(II)-K16A may suggest a kinetic barrier for amyloid to find the proper orientation for copper complexation.

Our TEM images were able to detect the presence of ribbon structures propagating within Cu(II)-K16A within 1 week, in contrast to the results of CD, which displayed no change in ellipticity indicative of beta-sheet formation within that timeframe. However, the detection threshold of circular dichroism is below that of TEM, which concentrates samples down within a specific area. As a result, we conclude that a detectable concentration of mature co-assembled Cu(II)-K16A is still consistent with the timescale provided from the CD data.

The Cu(II)-K16A system displayed a significantly higher reduction potential than free CuCl2 in buffer by a significant magnitude. The 732 mV vs. SHE reduction potential of co-assembled Cu(II)-K16A places it above most mononuclear cupredoxins and mimics the reduction potentials of high-potential laccases. We theorized that the high Cu(II) reduction potential within the co-assembled Cu(II)-K16A system stems from orbital strain of Cu(II)-peptide ligand coordination. We assign the Cu(II) within the system to be in an “entatic” state, in which metalloproteins display heightened reactivity compared to simple coordination complexes, from geometric strains imposed by the metal’s active site.

Evidence of slow electron transfer kinetics, along with a surprisingly linear Cottrell relationship of co-assembled Cu(II)-K16A, appears unusual, due to the slow diffusion kinetics of a nanoscale assembly. Due to the bulk of Cu(II)-K16A, along with its slow electron transfer kinetics, we predicted that it would have a slow mass transfer rate

and display a non-linear Cottrell relationship. However, a similar phenomenon of slow diffusing metalloproteins displaying linear Cottrell plots has been attributed to similarly bulky, slow-diffusing metal organic framework (MOF) assemblies, where charge hopping between metal centers is displayed, in which the coupled metal centers facilitate electron flux between the electrode and slow-diffusing bulk[36]. Therefore, we propose a similar charge-hopping mechanism to be taking place within the co-assembled Cu(II)-K16A system.

From the CD plots of $CuCl_2$ in buffer and within the co-assembled Cu(II)-K16A particles, it is evident that the electrochemistry of Cu within the respective system shows diminished reduction potential and redox activity than that of the matured co-assembled Cu(II)-K16A system. This supports the evidence that copper-amyloid interactions are responsible for redox potential elevation, along with degree of assembly maturation. This suggests that insufficient geometric strain is imposed on Cu(II) within the K16A particles to induce significant redox activity.

The presence of a broad peak between ~-20 mV to ~-100 mV is evident in the voltammograms of all chemically reversible samples. From literature, we attribute this peak to the reduction of O_2 to H_2O_2.[35] Though Cu(I)-K16A displayed the ability to produce H_2O_2 has been elucidated, further experiment is needed to confirm the potential of Cu(II)-K16A for hydrogen peroxide evolution. Numerous experiments were proposed to probe this; An Amplex Red assay of coassembled Cu(II)-K16A would have determined its rate of H_2O_2 production, while anaerobic CV and a coumarin fluorescence assay would have ruled out the potential of O_2 and $OH\bullet$ to the contribution of the broad peak. However, these experiments were cut short due to time constraints

from COVID-19. As a result, future experimentations with the previously proposed assays could definitively elucidate the chemical responsible for the broad peak.

Future experiments are necessary to fully characterize the interactions between copper and amyloid within the co-assembled Cu(II)-K16A system. As a result, electron spin echo envelope modulation (ESEEM) and X-ray absorption fine structure (XAFS0 fitting could assign clear geometric assignments to the position of ligands that the copper chelates to within the system, along with a quantitative assignment of copper density within the system. Understanding the coordination sphere of Cu(II)-K16A may grant us further insight into the unusual electrochemical reactivity of our metalloprotein. In addition, future experiments could determine the ability of Cu(II)-K16A to catalyze lignin degradation. Optimization of reaction conditions for lignin degradation could also allow for increased industrial viability of Cu(II)-K16A as an electrocatalyst.

REFERENCES CITED

1. Nastri, F.; D'Alonzo, D.; Leone, L.; Zambrano, G.; Pavone, V.; Lombardi, A. Engineering Metalloprotein Functions in Designed and Native Scaffolds. *Trends in Biochemical Sciences* **2019**, *44* (12), 1022–1040.
2. Putignano, V.; Rosato, A.; Banci, L.; Andreini, C. MetalPDB in 2018: a Database of Metal Sites in Biological Macromolecular Structures. *Nucleic Acids Research* **2017**, *46* (D1).
3. Lu Y, Berry SM, Pfister TD. Engineering novel metalloproteins: design of metal-binding sites into native protein scaffolds. *Chem. Rev*. **2001**, *101,* 3047–3080.

4. Burges BK, Lowe DJ. "Mechanism of Molybdenum Nitrogenase". *Chemical Reviews* **1996** (7), 2983–3011

5. Cronan, J. E. Biotin and Lipoic Acid: Synthesis, Attachment, and Regulation. *EcoSal* **2008**.
6. Watkins, D. W.; Jenkins, J. M. X.; Grayson, K. J.; Wood, N.; Steventon, J. W.; Vay, K. K. L.; Goodwin, M. I.; Mullen, A. S.; Bailey, H. J.; Crump, M. P.; Macmillan, F.; Mulholland, A. J.; Cameron, G.; Sessions, R. B.; Mann, S.; Anderson, J. L. R. Construction and in Vivo Assembly of a Catalytically Proficient and Hyperthermostable De Novo Enzyme. *Nature Communications* **2017,** *8* (1).
7. Zastrow, M. L.; Pecoraro, V. L. Designing Functional Metalloproteins: From Structural to Catalytic Metal Sites. *Coordination Chemistry Reviews* **2013**, *257* (17-18), 2565–2588.
8. Kou, S.; Yang, Z.; Luo, J.; Sun, F. Entirely Recombinant Protein-Based Hydrogels for Selective Heavy Metal Sequestration. *Polymer Chemistry* **2017**, *8* (39), 6158–6164.
9. Zhang, J.; Huang, X.; Zhang, R. K.; Arnold, F. H. Enantiodivergent α-Amino C–H Fluoroalkylation Catalyzed by Engineered Cytochrome P450s. *Journal of the American Chemical Society* **2019**, *141* (25), 9798–9802.
10. Hakulinen, N.; Rouvinen, J. Three-Dimensional Structures of Laccases. *Cellular and Molecular Life Sciences* **2015**, *72* (5), 857–868.
11. Chauhan, P. S.; Goradia, B.; Saxena, A. Bacterial Laccase: Recent Update on

Production, Properties and Industrial Applications. *3 Biotech* **2017**, 7 (5).

12. Cabana, H.; Jiwan, J.-L. H.; Rozenberg, R.; Elisashvili, V.; Penninckx, M.; Agathos, S. N.; Jones, J. P. Elimination of Endocrine Disrupting Chemicals Nonylphenol and Bisphenol A and Personal Care Product Ingredient Triclosan Using Enzyme Preparation from the White Rot Fungus Coriolopsis Polyzona. *Chemosphere* **2007**, *67* (4), 770–778.
13. Yessekin, B.; Bogachev, V. Water Resources and Sustainable Development in Central Asia: Roles of Risk Assessment and Risk Management. *Risk Assessment as a Tool for Water Resources Decision-Making in Central Asia* **2004**, 197–212.
14. Iark, D.; Buzzo, A. J. D. R.; Garcia, J. A. A.; Côrrea, V. G.; Helm, C. V.; Corrêa, R. C. G.; Peralta, R. A.; Regina De Fátima Peralta Muniz Moreira; Bracht, A.; Peralta, R. M. Enzymatic Degradation and Detoxification of Azo Dye Congo Red by a New Laccase from Oudemansiella Canarii. *Bioresource Technology* **2019**, 289, 121655.
15. Christopher, L. P.; Yao, B.; Ji, Y. Lignin Biodegradation with Laccase-Mediator Systems. *Frontiers in Energy Research* **2014**, *2*.
16. Bulter, T.; Alcalde, M.; Sieber, V.; Meinhold, P.; Schlachtbauer, C.; Arnold, F. H. Functional Expression of a Fungal Laccase in Saccharomyces Cerevisiae by Directed Evolution. *Applied and Environmental Microbiology* **2003**, *69* (2), 987–995.
17. Hortling, B.; Ranua, M.; Sundquist, J. Investigation of the Residual Lignin in Chemical Pulps. *Nordic Pulp & Paper Research Journal* **1990**, *5* (1), 33–3

18. Liu, Z.; Xie, T.; Zhong, Q.; Wang, G. Crystal Structure of CotA Laccase Complexed with 2,2-Azinobis-(3-Ethylbenzothiazoline-6-Sulfonate) at a Novel Binding Site. *Acta Crystallographica Section F Structural Biology Communications* **2016**, *72* (4), 328–335.
19. Bulter, T.; Alcalde, M.; Sieber, V.; Meinhold, P.; Schlachtbauer, C.; Arnold, F. H. Functional Expression of a Fungal Laccase in Saccharomyces Cerevisiae by Directed Evolution. *Applied and Environmental Microbiology* **2003**, *69* (2), 987–995.
20. Shleev, S.; Morozova, O.; Nikitina, O.; Gorshina, E.; Rusinova, T.; Serezhenkov, V.; Burbaev, D.; Gazaryan, I.; Yaropolov, A. Comparison of Physico-Chemical Characteristics of Four Laccases from Different Basidiomycetes. *Biochimie* **2004**, *86* (9-10), 693–703.
21. Bulter, T.; Alcalde, M.; Sieber, V.; Meinhold, P.; Schlachtbauer, C.; Arnold, F. H. Functional Expression of a Fungal Laccase in Saccharomyces Cerevisiae by Directed Evolution*. Applied and Environmental Microbiology* **2003**, *69* (2), 987–995.
22. Baldrian, P. Fungal Laccases – Occurrence and Properties. *FEMS Microbiology Reviews* **2006**, *30* (2), 215–242.
23. Guan, Z.-B.; Luo, Q.; Wang, H.-R.; Chen, Y.; Liao, X.-R. Bacterial Laccases: Promising Biological Green Tools for Industrial Applications. *Cellular and Molecular Life Sciences* **2018**, *75* (19), 3569–3592.
24. Sunde, M.; Serpell, L. C.; Bartlam, M.; Fraser, P. E.; Pepys, M. B.; Blake, C. C.

Common Core Structure of Amyloid Fibrils by Synchrotron X-Ray Diffraction Edited by F. E. Cohen. *Journal of Molecular Biology* **1997**, *273* (3), 729–739.

25. Jahn, Thomas R., et al. "The common architecture of cross-β amyloid." *Journal of Molecular Biology* **2010,** *395* (4), 717-727.

26. Eisenberg, D.; Jucker, M. The Amyloid State of Proteins in Human Diseases. *Cell* **2012**, *148* (6), 1188–1203.

27. Liang, Y.; Guo, P.; Pingali, S. V.; Pabit, S.; Thiyagarajan, P.; Berland, K. M.; Lynn, D. G. Light Harvesting Antenna on an Amyloid Scaffold. *Chemical Communications* **2008**, No. 48, 6522.

28. Omosun, T. O.; Hsieh, M.-C.; Childers, W. S.; Das, D.; Mehta, A. K.; Anthony, N. R.; Pan, T.; Grover, M. A.; Berland, K. M.; Lynn, D. G. Catalytic Diversity in Self-Propagating Peptide Assemblies. *Nature Chemistry* **2017**, *9* (8), 805–809.

29. Dong, J.; Canfield, J. M.; Mehta, A. K.; Shokes, J. E.; Tian, B.; Childers, W. S.; Simmons, J. A.; Mao, Z.; Scott, R. A.; Warncke, K.; Lynn, D. G. Engineering Metal Ion Coordination to Regulate Amyloid Fibril Assembly and Toxicity. *Proceedings of the National Academy of Sciences* **2007**, *104* (33), 13313–13318.

30. Maynard, Christa J., et al. "Metals and amyloid-β in Alzheimer's disease." *International Journal of Experimental Pathology* **2005,** *86* (3), 147-159.

31. Huang, Xudong, et al. "Cu (II) potentiation of Alzheimer Aβ neurotoxicity

correlation with cell-free hydrogen peroxide production and metal reduction." *Journal of Biological Chemistry* **1999,** *274* (52), 37111-37116.

32. Hernández-Guzmán, J.; Sun, L.; Mehta, A. K.; Dong, J.; Lynn, D. G.; Warncke, K. Copper(II)-Bis-Histidine Coordination Structure in a Fibrillar Amyloid β-Peptide Fragment and Model Complexes Revealed by Electron Spin Echo Envelope Modulation Spectroscopy. *ChemBioChem* **2013**, *14* (14), 1762–1771.
33. Mold, M.; Ouro-Gnao, L.; Wieckowski, B. M.; Exley, C. Copper Prevents Amyloid-β1–42 from Forming Amyloid Fibrils under near-Physiological Conditions in Vitro. *Scientific Reports* **2013**, *3* (1).
34. Mot, A. C.; Silaghi-Dumitrescu, R. Laccases: Complex Architectures for One-Electron Oxidations. *Biochemistry (Moscow)* **2012**, *77* (12), 1395–1407.
35. Hewitt, N.; Rauk, A. Mechanism of Hydrogen Peroxide Production by Copper-Bound Amyloid Beta Peptide: A Theoretical Study. *The Journal of Physical Chemistry B* **2009**, *113* (4), 1202–1209.
36. Ahrenholtz, S. R.; Epley, C. C.; Morris, A. J. Solvothermal Preparation of an Electrocatalytic Metalloporphyrin MOF Thin Film and Its Redox Hopping Charge-Transfer Mechanism. *Journal of the American Chemical Society* ***2014***, *136* (6), 2464–2472.